Author/s:
Neville, SL;Sjöhamn, J;Watts, JA;MacDermott-Opeskin, H;Fairweather, SJ;Ganio, K;Hulyer, AC;McGrath, AP;Hayes, AJ;Malcolm, TR;Davies, MR;Nomura, N;Iwata, S;O'Mara, ML;Maher, MJ;McDevitt, CA

Title:
The structural basis of bacterial manganese import

Date:
2021-08-01

Citation:
Neville, S. L., Sjöhamn, J., Watts, J. A., MacDermott-Opeskin, H., Fairweather, S. J., Ganio, K., Hulyer, A. C., McGrath, A. P., Hayes, A. J., Malcolm, T. R., Davies, M. R., Nomura, N., Iwata, S., O'Mara, M. L., Maher, M. J. & McDevitt, C. A. (2021). The structural basis of bacterial manganese import. Science Advances, 7 (32), https://doi.org/10.1126/sciadv.abg3980.

Persistent Link:
https://hdl.handle.net/11343/287627

BIOPHYSICS

The structural basis of bacterial manganese import

Stephanie L. Neville[1†], Jennie Sjöhamn[2†‡], Jacinta A. Watts[1†], Hugo MacDermott-Opeskin[3], Stephen J. Fairweather[3,4], Katherine Ganio[1], Alex Carey Hulyer[1], Aaron P. McGrath[2§], Andrew J. Hayes[1], Tess R. Malcolm[5], Mark R. Davies[1], Norimichi Nomura[6], So Iwata[6,7,8], Megan L. O'Mara[3], Megan J. Maher[2,5]*, Christopher A. McDevitt[1]*

Metal ions are essential for all forms of life. In prokaryotes, ATP-binding cassette (ABC) permeases serve as the primary import pathway for many micronutrients including the first-row transition metal manganese. However, the structural features of ionic metal transporting ABC permeases have remained undefined. Here, we present the crystal structure of the manganese transporter PsaBC from *Streptococcus pneumoniae* in an open-inward conformation. The type II transporter has a tightly closed transmembrane channel due to "extracellular gating" residues that prevent water permeation or ion reflux. Below these residues, the channel contains a hitherto unreported metal coordination site, which is essential for manganese translocation. Mutagenesis of the extracellular gate perturbs manganese uptake, while coordination site mutagenesis abolishes import. These structural features are highly conserved in metal-specific ABC transporters and are represented throughout the kingdoms of life. Collectively, our results define the structure of PsaBC and reveal the features required for divalent cation transport.

INTRODUCTION

The first-row transition element manganese (Mn) is essential for life (*1*, *2*). Manganese serves crucial roles in biological systems where it provides structural stability and/or catalytic activity for metalloproteins involved in diverse processes such as regulating carbon metabolism, oxidative stress tolerance, and, in pathogens, evasion of host defenses (*3*). Import of Mn^{2+} in prokaryotes is primarily facilitated by adenosine 5′-triphosphate (ATP)–binding cassette (ABC) permeases, although natural resistance-associated macrophage protein (NRAMP) and P-type adenosine triphosphatases (ATPases) have been shown to also contribute in specific microorganisms (*4*). Irrespective of the protein architecture, metal ion acquisition requires shielding of the charge from the lipid bilayer to enable transmembrane translocation. This can be achieved through the formation of metal chelate complexes as occurs in the import of iron (siderophore and heme), cobalt (cobalamin), and, in some instances, zinc (Zn; zincophore). However, a subset of type II ABC permeases directly transport ionic metals, such as Mn^{2+} and Zn^{2+}, into the cytoplasm, although there remains a paucity of information on the structural and molecular properties that facilitate this process.

Type II ABC permeases associated with metal ion import are composed of an ABC transporter, formed by two transmembrane domains (TMDs), two cytoplasmic nucleotide binding domains (NBDs), and an extra-cytoplasmic solute binding protein (SBP). The SBPs have high affinities for metal ion substrates, typically in the nanomolar to micromolar range (*5*), enabling efficacious capture in the extra-cytoplasmic space. SBP-mediated metal ion delivery to the transporter, in concert with ATP-driven active transport via the ABC transporter, provides an efficient pathway for the scavenging of poorly abundant environmental substrates (*6*). In the globally significant Gram-positive bacterial pathogen *Streptococcus pneumoniae* (the pneumococcus), PsaBCA is the type II ABC permease responsible for Mn^{2+} acquisition. *S. pneumoniae* has an absolute requirement for Mn^{2+} to mediate virulence and in vivo disease, and this is reflected in the near-absolute amino acid conservation of PsaC (TMD; 99.74%), PsaB (NBD; 99.91%), and PsaA (SBP; 99.83%) in an analysis of more than 20,000 pneumococcal genomes (fig. S1) (*7*). The structural and mechanistic features of PsaA that contribute to Mn^{2+} selectivity have been characterized (*8*, *9*), while the contribution of PsaBC remains undefined. Here, we aimed to determine the structure of PsaBC to elucidate the mechanistic bases of metal ion specificity and translocation.

RESULTS AND DISCUSSION

Recombinant wild-type (WT) PsaBC and a spontaneous PsaBC variant (PsaC:Phe^{100}Ser) were screened for overexpression, purification, and crystallization. The ^{F100S}PsaBC protein was successfully crystallized in two forms: (i) as a ^{F100S}PsaBC-Fab complex in space group $C222_1$ and (ii) ^{F100S}PsaBC alone in space group $P1$ (Fig. 1, A to C). Despite extensive efforts, ^{WT}PsaBC (either in complex with a Fab or alone) did not produce crystals suitable for data collection and structure solution. Refinements to 2.85- and 2.9-Å resolution, respectively, converged with residuals $R = 23.8$ and $R_{free} = 27.1$ for ^{F100S}PsaBC-Fab and $R = 26.0$ and $R_{free} = 28.1$ for ^{F100S}PsaBC. The final models show excellent geometries (table S1) (*10*).

The ^{F100S}PsaBC variant retained ATPase activity comparable to ^{WT}PsaBC, although Mn^{2+} transport functionality was impaired (Fig. 1, E to G). Notably, the ATPase activities of ^{WT}PsaBC and the ^{F100S}PsaBC variant were not stimulated by the presence of PsaA

---

[1]Department of Microbiology and Immunology, The Peter Doherty Institute for Infection and Immunity, The University of Melbourne, Melbourne, Victoria, Australia. [2]Department of Biochemistry and Genetics, La Trobe Institute for Molecular Science, La Trobe University, Melbourne, Victoria, Australia. [3]Research School of Chemistry, Australian National University, Canberra, ACT, Australia. [4]Research School of Biology, Australian National University, Canberra, ACT, Australia. [5]School of Chemistry and The Bio21 Molecular Science and Biotechnology Institute, The University of Melbourne, Melbourne, Victoria, Australia. [6]Department of Cell Biology, Graduate School of Medicine, Kyoto University, Kyoto, Japan. [7]Research Acceleration Program, Membrane Protein Crystallography Project, Japan Science and Technology Agency, Kyoto, Japan. [8]RIKEN SPring-8 Center, 1-1-1 Kouto, Sayo-cho, Sayo-gun, Hyogo, Japan.
*Corresponding author. Email: megan.maher@unimelb.edu.au (M.J.M.); christopher.mcdevitt@unimelb.edu.au (C.A.M.)
†These authors contributed equally to this work.
‡Present address: Institute for Biomedicine, Department of Infectious Diseases, and the Centre for Antibiotic Resistance Research, University of Gothenburg, Gothenburg, Sweden.
§Present address: Takeda California Inc., San Diego, CA, USA.

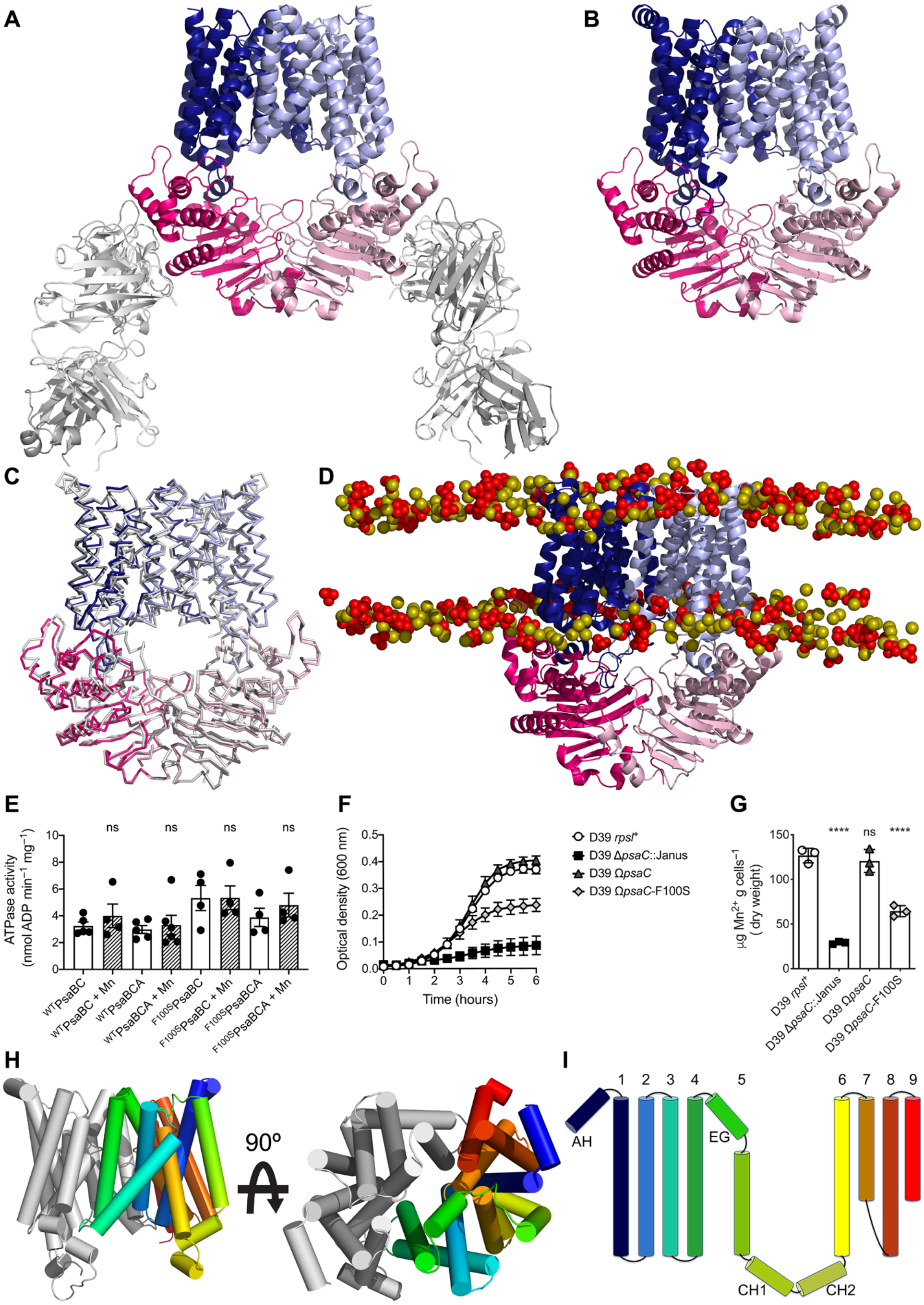

Fig. 1. Structure and activity of the PsaBC transporter. (**A**) ^{F100S}PsaB$_2$C$_2$-Fab$_2$ complex (space group $C222_1$; PsaC, blue and lavender; PsaB, hot and light pink; Fabs, gray). (**B**) ^{F100S}PsaB$_2$C$_2$ structure [space group $P1$; colored as in (A)]. (**C**) Superposition of ^{F100S}PsaB$_2$C$_2$-Fab$_2$ and ^{F100S}PsaB$_2$C$_2$ structures [^{F100S}PsaB$_2$C$_2$-Fab$_2$ colored as in (B); ^{F100S}PsaB$_2$C$_2$ in gray]. Fabs omitted for clarity. (**D**) MD snapshot of ^{WT}PsaB$_2$C$_2$ [colored as in (A)] in a PG and CDL membrane. Headgroups of lipid species (PG, yellow; CDL species, orange) are shown as spheres with tails hidden. (**E**) ATPase activity of reconstituted ^{WT}PsaBC and ^{F100S}PsaBC with Mn^{2+} and/or PsaA. Data represent means (± SEM) from at least four independent experiments. (**F**) Growth of WT *S. pneumoniae* (D39 *rpsl*$^{+}$), the isogenic mutant, and complemented strains (Ω) in Mn^{2+}-limited media. Data represent means (± SD) absorbance measurements from three independent experiments. (**G**) Mn^{2+} accumulation of *S. pneumoniae* strains in Mn^{2+}-limited media. Data represent means (± SD) from three independent experiments. Statistical significance was determined by one-way analysis of variance (ANOVA) with Tukey posttest $P > 0.05$, not significant (ns); ****$P < 0.0001$. (**H**) PsaC (from ^{F100S}PsaB$_2$C$_2$) with helices represented as cylinders. One monomer is colored gray, the other is colored from blue (N terminus) to red (C terminus). (**I**) Topology of PsaC monomers with helices numbered (AH, amphipathic helix; EG, extracellular gate; CH, coupling helix). Colors correspond to (H).

and/or Mn^{2+} (Fig. 1E). This observation is similar to other characterized type II ABC importers wherein the ATPase activity has been shown to be relatively uncoupled from the substrate occupancy status of the SBP (*11*–*13*). This is in stark contrast to type I ABC importers (*14*) and highlights the critical importance of metal ion release kinetics from the SBP PsaA (*8*, *9*, *15*) in contributing to specificity of permease import. The isogenic *S. pneumoniae* D39 ^{F100S}PsaBC strain grew in Mn^{2+}-limited media (Fig. 1F), but at a reduced growth rate and with significantly decreased Mn^{2+} accumulation relative to the WT and complemented strains, although to a lesser extent than the isogenic *psaC* deletion strain (Fig. 1G). This is attributable to the F100S mutation most likely affecting the dimensions and/or polarity of the translocation pore, rather than a significant structural change in the presence of the mutation [see discussion of molecular dynamics (MD) analyses below].

In the *C*222$_1$ structure, there is a single ^{F100S}PsaBC-Fab complex per asymmetric unit, with the ^{F100S}PsaB$_2$C$_2$-Fab$_2$ assembly generated by the application of crystallographic symmetry operators (Fig. 1A). The Fab fragments associate exclusively with the PsaB protomers (fig. S3A) through two surface-located helices (residues 109 to 122 and 174 to 184), with a total buried surface area for PsaB of 1033 $Å^2$. All crystal packing contacts throughout the crystal are mediated through Fab-Fab interactions (fig. S3B).

The ^{F100S}PsaBC structure shows four ^{F100S}PsaB$_2$C$_2$ assemblies per asymmetric unit (Fig. 1B). Although the crystals of ^{F100S}PsaBC were grown in the presence of adenylyl-imidodiphosphate (AMP-PNP) and $MgCl_2$, there was no electron density to indicate the presence of bound nucleotide in the crystal. The ^{F100S}PsaB$_2$C$_2$ unit from the ^{F100S}PsaBC-Fab structure superposes with each equivalent assembly within the asymmetric unit of the ^{F100S}PsaBC structure with an average root mean squared deviation (RMSD) of 0.9 Å, indicating only minor differences between the ^{F100S}PsaB$_2$C$_2$ assemblies within the ^{F100S}PsaBC-Fab and ^{F100S}PsaBC structures. Therefore, Fab binding results in minimal structural perturbations (Fig. 1C). In addition, each ^{F100S}PsaBC unit superposes with other ^{F100S}PsaBC assemblies within the asymmetric unit with an average RMSD of 0.5 Å (for 500 common Cα positions), indicating that all chains have very similar overall structures. Given these similarities, a single tetramer will be described to represent all ^{F100S}PsaB$_2$C$_2$ complexes for the *P*1 structure and used for the MD simulations of ^{F100S}PsaB$_2$C$_2$.

To identify any differences between the ^{F100S}PsaBC and ^{WT}PsaBC structures, an in silico reverse mutation was performed on the ^{F100S}PsaB$_2$C$_2$ structure to recover ^{WT}PsaB$_2$C$_2$. MD simulations (eight 500-ns replicas) were then performed for each structure embedded in a solvated *S. pneumoniae* membrane (*16*–*18*) composed of a 2:1 ratio of phosphatidylglycerol (PG) and cardiolipin (CDL) to assess the stabilities of the protein complexes in a membrane environment (Fig. 1D). The trajectories were combined, and the resulting analysis showed an average Cα RMSD of 3.0 ± 0.3 Å for the membrane-embedded protein complexes relative to their respective starting structures. Cluster analysis of the MD simulations showed that both ^{WT}PsaB$_2$C$_2$ and ^{F100S}PsaB$_2$C$_2$ complexes populated the same conformational cluster, as defined by a cutoff RMSD of 3.0 Å, for 96.7% of the total simulation time (cluster 1; fig. S2). The remaining 3.3% of the combined trajectories sampled three further conformational clusters, which are primarily attributable to changes in the relative orientations of flexible loop regions (clusters 2 to 4; fig. S2). Collectively, the MD analyses indicate that the ^{WT}PsaB$_2$C$_2$ and ^{F100S}PsaB$_2$C$_2$ complexes are stable in MD simulations, and both adopt the same overall conformation (movies S1 and S2). Further, the predicted structures in the membrane, with calculated RMSD values, are indicative of thermal fluctuations and no apparent global changes in protein conformation.

The ^{F100S}PsaB$_2$C$_2$ dimer contains 18 transmembrane helices (nine per protomer; Fig. 1H), a short N-terminal amphipathic helix, an extracellular gate (EG) helix, and two coupling helices (CH1 and CH2; Fig. 1I) and is relatively symmetrical. The ^{F100S}PsaC monomers dimerize through interactions between TM2, TM4 (including the EG helix), TM7, and TM9. TM2 (residues 41 to 62), TM4 (residues 92 to 113), and the EG (residues 117 to 125) line the ~30-Å-long translocation pathway (Fig. 2, A and B), which is created by the dimerization. Residues Ser^{117} and Thr^{118} are positioned at the extracellular surface of the translocation pore, with the entrance lined by residues Phe^{121}, Leu^{124}, and Phe^{125} from the EG, with π-π stacking between Phe^{121} and Phe^{125} (Fig. 2A). The roles of the EG residues Phe^{121} and Phe^{125} were investigated by mutagenesis. Phenotypic characterization of the isogenic *S. pneumoniae* mutant strains revealed that both the F121A and F125A strains were significantly perturbed for Mn^{2+} accumulation and growth under Mn^{2+}-limited conditions relative to control strains (fig. S4).

Below the pore entrance, the channel is restricted by the side chains of residues Leu^{104} (TM4) and Ile^{199} (from the loop bridging TM7 and TM8; Fig. 2, A to C). The diameter of the pore at this point reduces to 0.7 Å (Fig. 2B). Given the ionic radius of Mn^{2+} (0.83 Å), "closure" of the pore through this cluster of residues likely prevents adventitious entry of other cationic solutes (Mg^{2+} = 0.72 Å, Ca^{2+} = 1.00 Å, Fe^{2+} = 0.78 Å, Cu^{2+} = 0.73 Å, and Zn^{2+} = 0.74 Å) or water (H_2O = 2.75 Å) and/or prevents "reflux" of the Mn^{2+} ion during permeation. Thus, the narrow pore aperture in the ^{F100S}PsaBC crystal structure renders the translocation pathway effectively closed with respect to membrane permeation. This is supported by solvation analyses (eight 500-ns replicas) of the translocation pathway (Fig. 2D), which shows that the extracellular surface of the translocation pathway is exposed to bulk solvent, but water is completely excluded by the EG and the restriction point below. Water permeation increases and approaches bulk solvation below the restriction point, indicative of an "inward-open" conformation for ^{F100S}PsaBC (*19*, *20*). This conformation has been described for the structures of BhuUV, BhuUV-T (*19*) (*Burkholderia cenocepacia*), and MolAB (*20*) (*Haemophilus influenzae*) complexes, for which the periplasmic gates are also described as "closed." The restriction of the translocation pathway in the BhuUV-T structure is mediated by both a hydrophobic interaction and a salt bridge (between residues Asp^{200} and Arg^{204}) (*19*). Although the inward facing conformation of type II permeases was initially suggested to be an unstable and short-lived state (*21*), its repeated observation indicates that it may be a stable, resting state for some transporters.

On the cytoplasmic side of the pore restriction, at a distance of ~4.5 Å, is a negatively charged cavity, where residues Asp^{46} and His^{50} from each ^{F100S}PsaC monomer are located (Fig. 2, A and E, and fig. S5). This combination of residues is highly conserved in the TMDs of 52 functionally characterized Mn^{2+}- and Zn^{2+}-translocating ABC importers (Fig. 2A and fig. S6). This raises the possibility that these residues interact with the cation as part of the mechanism for metal ion translocation. In this conformation of the transporter, these residues are positioned 3.0 to 3.4 Å from the center of the translocation channel through which the Mn^{2+} ion traverses. Relatively subtle movements of TM2, facilitated by nucleotide and/or

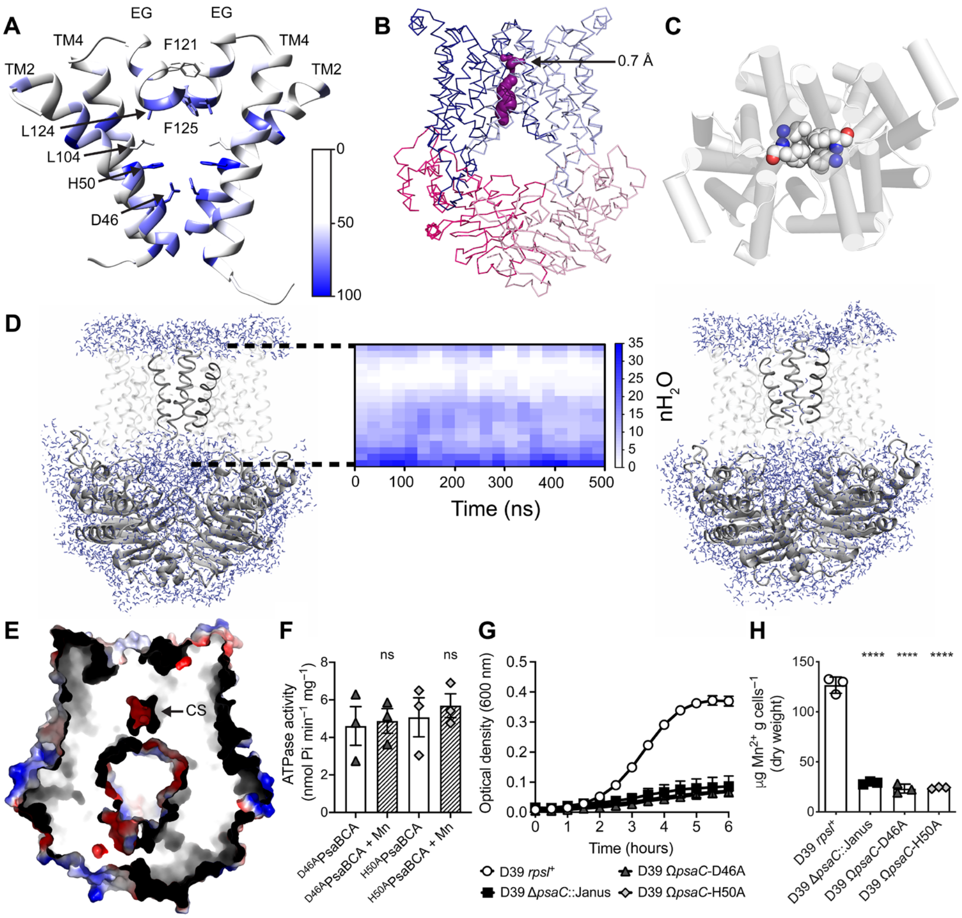

Fig. 2. The Mn^{2+} translocation pathway in PsaBC. (**A**) Structural elements composing the translocation pathway with Phe^{121}, Leu^{124}, Phe^{125}, Leu^{104}, His^{50}, and Asp^{46} shown as sticks. Residue conservation (65 TMDs from 52 characterized transporters; fig. S6) mapped to PsaC (<50%, white; 50 to 100%, white to blue). (**B**) Volume of the $^{F100S}PsaB_2C_2$ translocation pathway visualized in purple; arrow denotes 0.7-Å closure. (**C**) π-π stacking between Phe^{121} and Phe^{125}. (**D**) MD analysis of $^{WT}PsaB_2C_2$ in a solvated membrane (8 × 500-ns simulations). Representative starting (left) and final (right) frames with time-dependent water occupancy displayed as a heat matrix (middle) aligned to the structure (dashed lines). PsaB (gray cartoon), PsaC (TM2 and TM4; black ribbons), and water molecules (blue sticks). (**E**) Representation of $PsaB_2C_2$ with negatively charged surfaces in red, positive in blue, and uncharged in white. Cutaway reveals the CS (indicated by arrow). (**F**) ATPase activity of reconstituted ^{D46A}PsaBCA and ^{H50A}PsaBCA in the presence or absence of Mn^{2+}. Data represent means (± SEM) from three independent experiments. (**G**) Growth of WT *S. pneumoniae* (D39 *rpsl*$^+$) and the mutant strains in Mn^{2+}-limited medium. Data represent means (± SD) absorbance measurements from three independent experiments. (**H**) Mn^{2+} accumulation of *S. pneumoniae* strains in Mn^{2+}-limited media. Data represent means (± SD) from three independent experiments. Statistical significance was determined by one-way ANOVA with Tukey posttest [$P > 0.05$, not significant (ns); ****$P < 0.0001$].

PsaA binding, would position these side chains within the typical coordination distances (1.8 to 2.3 Å) associated with Mn^{2+}-protein complexes (*22*). Therefore, we refer to this cluster of residues as a coordination site (CS). We investigated the role of the CS residues by mutagenesis. Although mutation of the residues did not influence coupling of the PsaBC ATPase activity in the presence of Mn^{2+}-PsaA (Fig. 2F), the isogenic *S. pneumoniae* mutant strains showed severely perturbed growth and Mn^{2+} accumulation in Mn^{2+}-limited medium (Fig. 2, G and H). Together, these data show that the CS residues play a critical role in facilitating cytoplasmic Mn^{2+} acquisition.

"Selectivity filters" have been observed in the structures of a number of ion channels and transporters which translocate ionic substrates across the membrane. In these systems, the common mechanism for divalent ion selection involves complementary electrostatic interactions between channel residues and the cationic substrate. For example, in the $Ca_v1.1$ ion channel, rings of four Glu residues and eight carbonyl oxygens provide a Ca^{2+} selective filter (*23*). Likewise, in the cardiac RyR, three rings each containing four acidic residues select for the permeation of solvated Ca^{2+} ions (*24*). In P-type ATPases such as the sarcoplasmic reticulum Ca^{2+} ATPase, polar interactions between Ca^{2+} ions and the carbonyl groups and side chains of surrounding amino acids have been observed (*25*).

Transition metal ion channels and transporters use additional metal coordination interactions, rather than solely relying upon electrostatics, to facilitate membrane traversal. For example, the eukaryotic Cu^+ channel Ctr1 includes two rings of Met residues that are proposed to specifically coordinate Cu^+ during its translocation, providing both a driving force for ion movement and a molecular mechanism for selectivity. The crystal structure of the SLC11 (NRAMP) transporter from *Staphylococcus capitis* (*Sca*DMT)—which transports Fe^{2+}, Mn^{2+}, and Cd^{2+} ions—includes a metal binding site composed of Met, Asp, and Asn residues, in addition to the carbonyl group from the polypeptide backbone as coordinating ligands. This CS is located in the unwound regions of two symmetry-related helices in the center of the bilayer. These residues were shown to be fully conserved in this class of transporter (including that from human) with their mutagenesis attenuating transport activity and metal binding affinities of the transporter (*26*). Lastly, cation diffusion facilitator proteins (CDFs), such as the bacterial Zn^{2+} transporter YiiP, have conserved sequence motifs (combinations of Asp and His residues) that coordinate the divalent metal during the transport cycle and vary in combination, with an associated alteration in the relative metal specificities, between Zn^{2+} and Mn^{2+} transporters (*27*, *28*).

Succinctly, the observation of ion coordinating residues in the translocation pathways of ion channels and transporters is not unusual. Further, substrate recognition sites within the translocation pathways of type I ABC permeases, such as the *Escherichia coli* maltose transporter $MalFGK_2$, have also been reported (*29*, *30*). However, the observation of a binding site within a type II ABC transporter is entirely unique, given that prevailing models hold that the translocation pathways of these transporters show no affinity for their transported substrates (i.e., that these transporters contain "Teflon" cavities) (*31*). For example, although the BhuUV complex transports the iron-chelate heme, no amino acid side chains with chemistries compatible with heme iron ligation—such as His, Cys, Tyr, or Met—are present within the translocation pathway. In contrast, we propose that in PsaBC, residues Asp^{46} and His^{50} form a CS within the Mn^{2+} translocation pathway, to provide an additional degree of specificity for Mn^{2+} uptake, in addition to the precise cation release that occurs via the interaction between PsaC and Mn^{2+}-bound PsaA. The presence of both Asp and His residues within the PsaC CS is consistent with the observation of these residues in the Zn^{2+} and Mn^{2+} binding sites of CDFs (*27*) and residues that commonly comprise the active sites of Mn^{2+}-dependent enzymes (*22*).

Below the CS is a cytoplasmic gate, composed of residue Leu^{43} from each PsaC protomer, and a pair of Asp^{93} residues below, exposed on the cytoplasmic side of the membrane. These residues presumably act to gate and/or drive metal ion translocation to the cytoplasm. The interaction between the ^{F100S}PsaC and PsaB dimers features two PsaC coupling helices (CH1 and CH2; Fig. 1I) that extensively interact with the corresponding PsaB protomers. In the structures of other type II ABC transporters, these helices have been proposed to play a role in the transmission of conformational change of the NBDs to the TMDs in response to nucleotide binding and hydrolysis (*12*, *19*, *20*, *32*, *33*).

Building on the identification of the CS (within TM2) and the EG (within TM4) as features crucial to facilitate cation translocation within the ABC transporter architecture, we examined the conservation of these motifs within the Pfam database of protein families (*34*). PsaC belongs to the ABC-3 transport family [Pfam v33.1 identifier PF00950 (*34*)], for which there are no structures publicly available. The ABC-3 transport family (PF00950) is composed of more than 10,000 sequences with an average length of 251 amino acids (interquartile range, 250 to 269 amino acids) and an average identity of 27%. Amino acid likelihood plots derived from the ABC-3 family alignment revealed high conservation of the TM2-TM4 TMDs across both Eubacteria and Archaea (figs. S7 and S8). Further, and in contrast to most of the other prokaryotic ABC importers (*35*), putative transporters encoded by the plastid genomes of several glaucophyte and rhodophyte species were also found to contain TM2-TM4 homologous regions (fig. S7). With the sole exception of *Porphyridium purpureum*, these eukaryotic plastid genomes were found to lack the PAM71-type and CMT1-type Mn^{2+} transporters common to plastids of other algae and plants (*36*). Although this is suggestive of a potential functional role for these ABC transporters in Mn^{2+} uptake, it is notable that the plastid genomes did not encode a corresponding ortholog for a metal-specific SBP, which is required for prokaryotic metal import and is typically encoded within the ABC permease operon. This may suggest a mechanistic difference in how the algal ABC transporter variants recruit putative metal substrates (Mn^{2+} and/or Zn^{2+}), although definitive studies remain to be conducted. Irrespective, the TM2-TM4 structural elements are highly conserved and appear to have been retained during algal plastid evolution, most likely arising from endosymbiotic origin and/or horizontal gene transfer events.

A search of the coordinates of the PsaC structure versus the Protein Data Bank (PDB) reveals that the most similar structures are the TMDs from the type II ABC transporter family (Fig. 3A and table S2) (*12*, *19*, *20*, *32*). However, PsaC has 9 TM helices, whereas other members of this family have 10. The reduced number of TM helices and the tight packing between PsaC protomers result in an overall more compact structure (Fig. 3A). Similarly, the PsaB structure is not only comparable to the NBDs of the type II ABC transporter family, such as BhuV and BtuD [10,20], but also unexpectedly shows similarity to the NBDs of the cobalt energy-coupling transporter from *Rhodobacter capsulatus* [CbiO (*37*)] and the unusual lipopolysaccharide transporter from *E. coli* [LptB (*38*); table S2]. Despite the structural similarity between these NBDs, their relative orientations are unique. The PsaB subunits and the motifs responsible for nucleotide binding and hydrolysis (i.e., the P loops, Walker motifs, and ABC signatures) are well separated in the PsaBC structure, so that they are offset relative to each other, parallel to the membrane plane [the distance between the Cα atoms of PsaB residues 40 (P loop) and 136 (ABC motif) is ~25 Å; Fig. 3A]. This is substantially different from the positioning of the structurally homologous NBDs in the BhuUV (*19*) complex where the P loop and ABC motif are well aligned for nucleotide binding {the equivalent distance in the BhuUV structure [PDB 5B58 (*19*)] is ~8.5 Å; Fig. 3B}. In the case of PsaBC, a substantial realignment of the PsaB monomers would therefore be required for ATP binding and hydrolysis. Given that the association of Mn^{2+}-PsaA with the PsaBC transporter appears uncoupled from the ATP hydrolysis, nucleotide binding rather than SBP docking most likely drives this rearrangement. However, the alignment of the NBDs would require a substantial movement (~15 Å) of both these domains and the TMDs, which may be linked to the relatively low rate of ATP hydrolysis observed for PsaBC.

The structure of ^{F100S}PsaBC provides an original snapshot of the mechanisms by which very small (<150 Da), charged entities, such as transition metal ions, are translocated across biological membranes in a specific and exquisitely controlled manner. Specificity for Mn^{2+} transport by PsaBC is engendered by the combination of metal ion binding and release kinetics by the SBP PsaA and the unique features of the type II ABC transporter PsaBC. Distinct from other type II transporters characterized to date, metal import is controlled and reflux prevented, by closure of the transmembrane pore in the inward-open conformation of the transporter. Inward transport of the metal ion is achieved by virtue of the CS within the

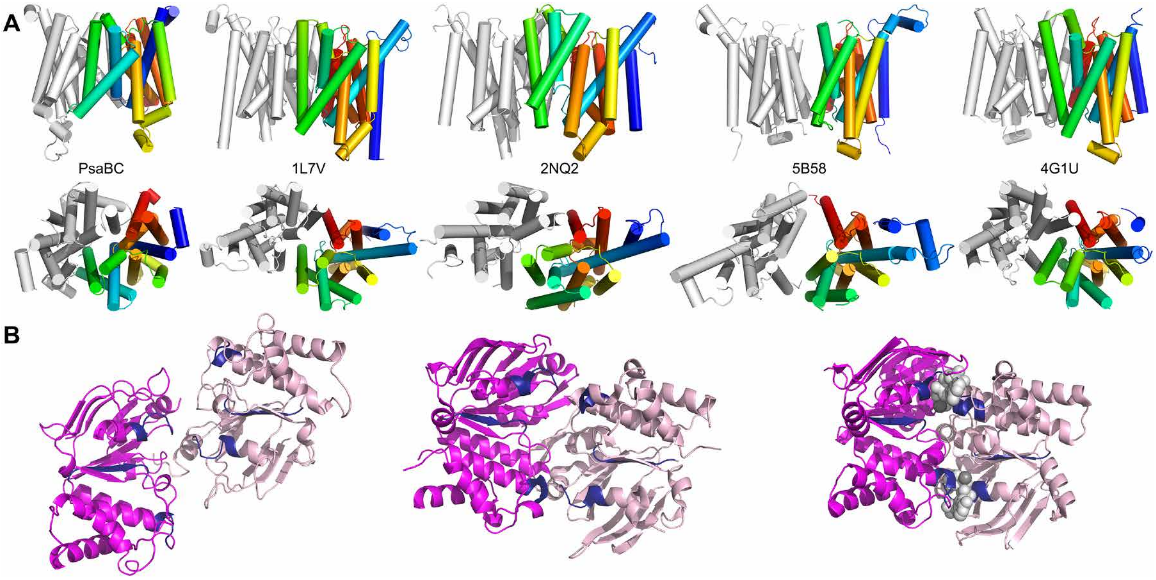

Fig. 3. Comparison of the ^{F100S}PsaB$_2$C$_2$ structure with those of other permeases. (**A**) The structures of the TMDs of ^{F100S}PsaB$_2$C$_2$ and homologs are shown in cartoon representations, with one monomer colored gray and the other from blue at the N terminus to red at the C terminus. Helices are shown as cylinders. The bottom representation is a rotation of the top view by 90°, parallel to the membrane plane. From left to right: ^{F100S}PsaC (this work), BtuC (*32*) (*E. coli*; PDB 1L7V), MolA (*20*) (*H. influenzae*; PDB 2NQ2), BhuU (*19*) (*B. cenocepacia*; PDB 5B58), and HmuU (*12*) (*Yersinia pestis*; PDB 4G1U). (**B**) Alignment of the NBD structures. From left to right: PsaB (this work), BhuV [23] (PDB 5B58), and CbiO [35] (*R. capsulatus*; PDB 5X40). In all panels, the NBD monomers are shown in magenta and light pink, and the ABC, Walker B, and P loop residues are highlighted in dark blue. For the CbiO structure, the bound nucleotide and magnesium ion are shown as gray spheres.

translocation pathway and the combination of the uncoupling and slow rate of ATP hydrolysis, which can likely be attributed to the unusual relative positioning of the NBDs. The selective acquisition of specific transition metal ions is essential to fundamental chemical processes in biological systems throughout the kingdoms of life. In contrast to other nutrients transported by ABC permeases—such as sugars, amino acids, peptides, vitamins, and osmolytes—metal ions are not "consumed" within cells. Hence, their uptake is precisely controlled according to the intracellular requirements, dictated by the tight regulation of permease expression, with the only other regulatory mechanisms arising through the actions of metal ion efflux pathways. The structure of PsaBC encapsulates the molecular mechanisms by which a delicate balance of cellular metal ion requirements can be achieved. Further, it highlights the structural and mechanistic diversity that exists within the ABC transporter superfamily. To date, the mechanistic differences within the type II ABC transporter grouping have been proposed to arise from the differences in substrate size, based on comparisons between the BtuCD (vitamin B12; 1355 Da) and MolBC (molybdate; 159 Da) transporters (*33*), although further structures are required to clarify the veracity of this inference. The structural and functional insights provided by PsaBC expand our knowledge of variations to the type II transport mechanism (fig. S9) and, crucially, potentially represent a new transporter class, comprising cation translocation elements present in all the kingdoms of life (*39*).

MATERIALS AND METHODS

Materials

Tryptone and yeast extract were purchased from Bacto (NSW, Australia). Complete, EDTA-free protease inhibitor tablets were obtained from Roche (Sigma-Aldrich, NSW, Australia). Deoxyribonuclease I from bovine pancreas was purchased from Sigma-Aldrich (NSW, Australia). *n*-Dodecyl-β-D-maltopyranoside (DDM) was obtained from Anatrace (Ohio, USA). Ni Sepharose high-performance histidine-tagged protein purification resin (HP resin) was purchased from GE Healthcare (NSW, Australia). Total *E. coli* lipid extract and egg L-α-phosphatidylcholine (egg PC) were obtained from Avanti Polar Lipids (Alabama, USA). Transition metal ion salts manganese(II) sulfate monohydrate, zinc(II) sulfate heptahydrate, copper(II) sulfate heptahydrate, cobalt(II) chloride, and nickel(II) chloride were purchased from Sigma-Aldrich (NSW, Australia). The Transcreener ADP2 FP Assay Kit was obtained from Bellbrook Labs (Wisconsin, USA).

Bacterial strains, culturing, and growth experiments

The *S. pneumoniae* mutant strains (table S3) were constructed using the Janus cassette (*40*). Briefly, the *rpsL* gene of *S. pneumoniae* D39 was replaced with a streptomycin-resistant allele (D39 *rpsl*$^+$) to allow counter selection. The upstream and downstream flanking regions of *psaC* were then amplified using primers (table S4) with complementarity to the Janus cassette and were joined to the Janus cassette by overlap extension polymerase chain reaction (PCR). These linear fragments were used to replace *psaC* in the *S. pneumoniae* D39 chromosome by homologous recombination. Exchange of the Janus cassette with mutant variants of *psaC* was achieved via homologous recombination. *S. pneumoniae* WT and mutant strains were routinely grown at 37°C with 5% CO$_2$ on blood agar [39 g liter^{-1} Columbia base agar (Oxoid) and 5% (v/v) defibrinated horse blood] or in THY [Todd-Hewitt broth (Oxoid) and 0.5% (w/v) Bacto yeast extract (Becton Dickinson and Company)]. For phenotypic assays, including growth kinetic assays and metal accumulation analyses, *S. pneumoniae* strains were grown in a Mn^{2+}-limited cation-defined medium with casein hydrolysate and 0.5% yeast extract, as described previously (*41*). Metal content of the Mn^{2+}-limited medium was determined by inductively coupled plasma mass spectrometry (ICP-MS) on an Agilent 8900 Triple Quadrupole ICP-MS as previously described (*8*, *42*) with the Mn^{2+}-limited cation-defined medium routinely containing <1 μM Mn^{2+}. Growth media were supplemented with the following antibiotics (Merck) where appropriate: erythromycin (0.2 μg ml^{-1}), chloramphenicol (6 μg ml^{-1}), streptomycin (150 μg ml^{-1}), gentamicin (5 μg ml^{-1}), or kanamycin (50 μg ml^{-1}). *E. coli* strains were routinely grown at 37°C in LB broth or on LB 1.5% agar plates supplemented with kanamycin (50 μg ml^{-1}) to maintain plasmids. Growth kinetic assays were performed using cultures of *S. pneumoniae* D39 and mutant variants prepared from overnight growth on blood agar supplemented with 30 μM Mn^{2+} and appropriate antibiotics, resuspended, and inoculated into the Mn^{2+}-limited medium to an optical density at 600 nm (OD_{600}) of 0.05. The culture was incubated at 37°C + 5% CO_2 and grown to OD_{600} = 0.3. Growth kinetic assays were conducted in a 96-well plate format using a FLUOstar Omega spectrophotometer (BMG Labtech). *S. pneumoniae* were inoculated in a final volume of 200 μl in the Mn^{2+}-limited medium (± supplementation where indicated) to a starting OD_{600} = 0.01 in a clear 96-well plate (Greiner). The plate was incubated at 37°C + 5% CO_2 for >16 hours, with readings taken every 30 min. All analyses were carried out to at least $n = 5$ biological replicates and data analyzed using GraphPad Prism (version 8).

Protein expression and purification

Sequences encoding *psaB* (UniProtKB, A0A0H2ZNF3) and *psaC* (UniProtKB, A0A0H2ZPI2) were amplified using standard PCR as overlapping open reading frames from *S. pneumoniae* D39 genomic DNA using the primers 5pPsaXhoI and 3pPsaKpnI (table S4). The amplified *psaBC* insert was gel purified, digested, and ligated into predigested pWaldo vector (*43*) between Xho I and Kpn I restrictions sites, upstream of a sequence encoding a tobacco etch virus (TEV) protease site and enhanced green fluorescent protein (eGFP)–8xHis. The resultant vector was used to concurrently express the untagged PsaB and the PsaC protein that was attached to a C-terminal fusion of eGFP-8xHis. This cloning strategy resulted in two constructs encoding (i) the WT PsaBC sequence (pWALDO-^{WT}PsaBC) and (ii) a “spontaneous” mutant in PsaC, F100S (pWALDO-^{F100S}PsaBC) (table S5). The ^{WT}PsaBC-TEV-GFP-His and ^{F100S}PsaBC-TEV-GFP-His proteins were overexpressed in *E. coli* BL21 (DE3) cells grown at 37°C in LB, supplemented with kanamycin (100 μg ml^{-1}) to an OD_{600} of 0.6, induced with isopropyl β-D-1-thiogalactopyranoside (0.2 mM), and harvested after 16 hours at 16°C. Cell pellets were suspended in binding buffer {20 mM tris-HCl (pH 8.0), 200 mM NaCl, and 1 mM TCEP [tris(2-carboxyethyl) phosphine hydrochloride]} and disrupted by passage through a TS series bench-top cell disruptor (Constant Systems Ltd.) at 35 kpsi. The membrane fraction was pelleted by ultracentrifugation (158,000*g*, 90 min, 4°C; Beckman Coulter Type 45 Ti rotor). The isolated membranes were resuspended in binding buffer [80 ml, 20 mM tris-HCl (pH 8.0), 200 mM NaCl, and 1 mM TCEP] and stirred at 4°C (1 hour) in the presence of DDM [1% (w/v) final concentration; Anatrace], followed by centrifugation (158,000*g*, 30 min, 4°C). The resulting supernatant (membrane extract) was incubated with Ni-Sepharose 6 Fast Flow resin (20 ml, GE Healthcare) preequilibrated with binding buffer, with stirring at 4°C (60 min). The resin was washed with increasing concentrations of sodium imidazole (20 and 40 mM, respectively) in DDM detergent buffer [20 mM tris-HCl (pH 8.0), 200 mM NaCl, 1 mM TCEP, and 0.03% (w/v) DDM] before elution (250 mM sodium imidazole in DDM detergent buffer).

To cleave the GFP-His tag from the ^{F100S}PsaBC-GFP-His fusion, TEV protease (5 mg) was added to the eluted protein, and the protein mixture was dialyzed against DDM detergent buffer (2 liters) at 4°C overnight. The cleaved ^{F100S}PsaBC protein was separated from the uncleaved species by reverse binding to Ni-Sepharose 6 Fast Flow resin (1 ml), preequilibrated with DDM detergent buffer. The ^{F100S}PsaBC protein was concentrated to a volume of 5 ml [100-kDa molecular weight cutoff (MWCO) Amicon Ultra concentrator, Merck Millipore] and injected onto a HiLoad 16/60 Superdex 200-pg column (GE Healthcare), preequilibrated with Cymal-6 detergent buffer [20 mM tris-HCl (pH 8.0), 200 mM NaCl, 1 mM TCEP, and 0.1% (w/v) Cymal-6 (Anatrace)]. The main peak fraction was concentrated to 20 mg ml^{-1} (100-kDa MWCO Amicon Ultra concentrator, Merck Millipore) before storage of the purified protein at −80°C.

Whole-cell ICP-MS

Elemental analysis of *S. pneumoniae* D39 and the mutant variants was performed in the Mn^{2+}-limited medium using culturing conditions described above. Bacterial cells were harvested at OD_{600} ~0.3 and then washed twice with phosphate-buffered saline (PBS) + 5 mM EDTA and twice with PBS. Cells were again pelleted, the supernatant was removed, and the pellet was desiccated overnight on a heat block at 96°C. Metal ion content was released by treatment with 1 ml of 35% nitric acid (HNO_3, Suprapur, Merck) at 96°C for 1 hour. Metal content was analyzed on an Agilent 8900 Triple Quadrupole ICP-MS (*42*, *44*). Bacterial growth for ICP-MS analyses was performed with two technical replicates in three independent biological experiments.

Fab generation and purification of the ^{F100S}PsaBC-fab complex

All the animal experiments conformed to the guidelines of the Guide for the Care and Use of Laboratory Animals of Japan and were approved by the Kyoto University Animal Experimentation Committee (approval number MedKyo18078). Mouse monoclonal antibodies against ^{F100S}PsaBC were raised according to the previous method (*45*). Briefly, a proteoliposome antigen was prepared by reconstituting purified, functional ^{F100S}PsaBC at high density into phospholipid vesicles consisting of a 10:1 mixture of egg PC (Avanti Polar Lipids) and the adjuvant lipid A (Sigma-Aldrich) to facilitate immune response. BALB/c mice were immunized with the proteoliposome antigen using three injections at 2-week intervals. Antibody-producing hybridoma cell lines were generated using a conventional fusion protocol. Hybridoma clones producing antibodies recognizing conformational epitopes in ^{F100S}PsaBC were selected by an enzyme-linked immunosorbent assay (ELISA) on immobilized phospholipid vesicles containing purified ^{F100S}PsaBC (liposome ELISA), allowing positive selection of the antibodies that recognized the native conformation of ^{F100S}PsaBC. Additional screening for reduced antibody binding to SDS-denatured ^{F100S}PsaBC was used for negative selection against linear epitope-recognizing antibodies. Stable complex formation between ^{F100S}PsaBC and each antibody clone was checked using fluorescence-detection size exclusion chromatography. Whole immunoglobulin G molecules, collected from the large-scale culture supernatant of monoclonal hybridomas and purified using protein G affinity chromatography, were digested with papain, and Fab fragments were isolated using a HiLoad 16/600 Superdex 200 pg gel filtration column followed by protein A affinity chromatography. The sequence of the Fab was determined via standard 5′ rapid amplification of complementary DNA ends using total RNA isolated from hybridoma cells.

The ^{F100S}PsaBC-Fab complex was generated by incubating ^{F100S}PsaBC (2.0 mg) with 2.0 molar equivalents of purified Fab on ice (1 hour), followed by separation of the ^{F100S}PsaBC-Fab complex from Fab alone by size exclusion chromatography (Superdex 200 Increase 10/300 GL, GE Healthcare) in Cymal-6 detergent buffer. Fractions confirmed to contain the complex were pooled and concentrated to 10 mg ml^{-1} for crystallization trials.

Protein crystallization and data collection

Crystallization trials for the ^{F100S}PsaBC protein and the ^{F100S}PsaBC-Fab complex were conducted using commercially available screens (MemGold and MemGold2, Molecular Dimensions) (*46*, *47*) by sitting drop vapor diffusion in 96-well plates (Molecular Dimensions) using protein samples at 10 mg ml^{-1} in Cymal-6 detergent buffer. Crystallization drops, consisting of equal volumes (0.2 μl) of reservoir and protein solutions, were dispensed using a Crystal Gryphon Liquid Handling System (Art Robbins Instruments) and were equilibrated against a reservoir of screen solution (50 μl). Plates were incubated at 20°C.

Optimization of initial crystallization conditions was carried out by hanging-drop vapor diffusion in 24-well VDX plates (Hampton Research). Diffraction-quality crystals of ^{F100S}PsaBC grew after 4 to 7 days at 20°C by hanging-drop vapor diffusion with drops containing equal volumes (1 μl) of ^{F100S}PsaBC [10 mg ml^{-1}, in Cymal-6 detergent buffer, 1 mM AMP-PNP (Sigma-Aldrich), and 5 mM $MgCl_2$] and crystallization solution [0.1 M MES (pH 6.5), 0.2 M $CaCl_2 \cdot 2H_2O$, and 33% (v/v) PEG400] equilibrated against crystallization solution (500 μl). The ^{F100S}PsaBC-Fab complex was crystallized at 20°C by hanging-drop vapor diffusion with drops consisting of equal volumes (1 μl) of protein (10 mg ml^{-1} in Cymal-6 detergent buffer) and reservoir solution [50 mM tris-HCl (pH 8.5) and 28% (v/v) PEG400]. Both the ^{F100S}PsaBC and ^{F100S}PsaBC-Fab crystals were flash-cooled in liquid nitrogen before data collection.

Diffraction data were recorded on a Dectris Pilatus 6M detector at the Stanford Synchrotron Radiation Laboratory, beamline 12-2. All data were collected at 100 K and were processed and scaled with HKL2000 (*48*). Data collection statistics are detailed in table S1.

Structure determination and refinement

The ^{F100S}PsaBC-Fab complex structure was solved by molecular replacement (MR) using PHASER with models derived from the NBD of the MolAB transporter (PDB 2NQ2) (*20*) and a synthetic Fab (PDB 2R8S) (*49*). The PsaBC component of the refined structure of ^{F100S}PsaBC-Fab was used to solve the structure of ^{F100S}PsaBC by MR using PHASER. Both structures were refined with REFMAC5 and PHENIX, using anisotropically corrected diffraction data with translation/liberation/screw (TLS), and manual model building was carried out with COOT (*50*). Tight non-crystallographic symmetry (NCS) restraints were applied for early cycles of refinement for the ^{F100S}PsaBC structure and were released for the final cycles. The quality of the structures was determined with MOLPROBITY (table S1) (*10*).

Reconstitution of PsaBC into proteoliposomes

Expression of ^{WT}PsaBC and mutant derivatives thereof for reconstitution and characterization used a GST-PsaBC-GFP-His fusion protein derived from the parental pWALDO-^{WT}PsaBC construct (table S5) and were purified using the protocol described above. PsaBC fusion proteins were incorporated into preformed proteoliposomes, composed of *E. coli* lipids:egg PC (3:1), using the previously described methods (*11*, *51*). Recombinant PsaA, purified using the established method (*8*), and Mn^{2+} were incorporated into proteoliposome lumens by freeze-thaw cycling. Reconstitution efficiency of PsaBC averaged 62.1 ± 3.2%, corresponding to 1.24 mg of PsaBC per 100 mg of lipid. PsaA was incorporated into proteoliposomes at a 50-fold molar excess of PsaBC, corresponding to a concentration of 13.1 to 25.0 μM, while Mn^{2+} was enclosed at a 10-fold molar excess relative to PsaA (131 to 250 μM). Michaelis-Menten parameters of the ATPase activity were determined by measuring the increase in concentration of adenosine 5′-diphosphate (ADP) as a function of ATP concentration (0.15 to 2 mM). ATPase activity was determined using the Transcreener ADP^2 FP Assay Kit (Bellbrook), wherein liberated ADP binds preferentially to an antibody-ADP-fluorophore complex. Activity was quantified in the presence or absence of PsaA and Mn^{2+} with background correction performed relative to empty proteoliposomes. TEV cleavage of the fusion tags did not significantly affect reconstitution efficiency or relative ATPase activity. All experiments were repeated at least three times, and data were fitted to Michaelis-Menten kinetics to calculate K_m and V_{max} values using GraphPad Prism (version 8).

PsaBCA conservation analysis

A global database of 20,020 publicly available *S. pneumoniae* genome sequences derived from the Global Pneumococcal Sequencing project (www.pneumogen.net) (*7*) was assembled by the Wellcome Sanger Institute Pathogen Informatics pipeline (*52*). The *S. pneumoniae* D39 genome (National Center for Biotechnology Information identifier NC_008533) served as the reference genome to determine the presence, amino acid sequence, and alignment of spd_1461 (*psaB*), spd_1462 (*psaC*), and spd_1463 (*psaA*) across the 20,020 clinical isolates using the screen_assembly script (*53*) and BLASTN v2.9.0 with parameters of 80% coverage and 80% identity. Amino acid variation was determined using MUSCLE alignment in Geneious Prime (*54*, *55*). Sequence conservation was determined by the percentage of variant amino acids compared to consensus.

Sequence conservation within known cation importers

Sixty-five sequences of the TMDs from 52 functionally characterized bacterial cation ABC transporters (table S6) were curated, and a multiple sequence alignment was performed using hmmalign (www.hmmer.org; hmmer version 3.3.1), with the ABC-3.hmm from Pfam PF00950 supplied as the alignment model (data file S2) (*34*). The sequence alignment corresponding to chains F and H of the *S. pneumoniae* PsaC (Spn_PsaC) structure was loaded into UCSF Chimera (*56*) to visualize sequence conservation relative to protein structure. Percent conservation of residues was then visualized with the command rangecolor mavPercentConserved 50 white 100 blue. The alignment was also used to generate an hmm for production of a logoplot using skylign.org (*57*). Full alignments in aligned FASTA format are provided in data file S1. Alignments were visualized using Jalview with identity coloring (*58*).

Sequence conservation of PF00950

The hmm from PF00950 (data file S2) was used to generate a logoplot using skylign.org (*57*). Logoplot was generated using information above background and consensus coloring. To determine the raw conservation of each residue within the 10,041 sequences identified in PF00950, the aligned sequences were obtained from PFAM and conservation mapped to the corresponding residues in the *S. pneumoniae* PsaC structure. Percent conservation of residues was then visualized with the command rangecolor mavPercentConserved 30 white 90 blue. These represented the average (30) and maximum (90) % conservation in the alignment.

To visualize the conservation of the PF00950 family across domains, representative sequences of bacteria, archaea, and eukaryote (algal plastid) sequences were obtained from UniProt (table S6). These include the 12 available algal plastid sequences for rhodophytes and glaucophytes, while representative archaea sequences ($n = 7$) were obtained by searching for ABC-3 protein family sequences and selecting the sequences with a predicted gene identity and function consistent with a cation transporter. Eubacterial sequences ($n = 12$) were selected from the alignment of the 65 sequences above (data file S3) with differing species and gene IDs prioritized for diversity. Multiple sequence alignment was performed using hmmalign (www.hmmer.org; hmmer version 3.3.1), with the ABC-3.hmm from PF00950 supplied as the alignment model (data file S2).

Simulation methodology

All simulation in this work was conducted using GROMACS2018 (*59*–*61*) under periodic boundary conditions, with the GROMOS 54A7 forcefield (*62*). The temperature of the system was maintained at 310 K by coupling to an external bath using the Bussi thermostat (*63*) with a temperature coupling constant of 0.1 ps. The lipid and nonlipid components of the system were coupled separately. The pressure of the system was maintained at 1 bar with semi-isotropic pressure coupling and a coupling constant of 0.5 ps. A Berendsen barostat (*64*) was used for equilibration to ensure stabilization of the box volume, followed by a Parrinello-Rahman barostat (*65*, *66*) for production simulation. A timestep of 2 fs was used for all simulations along with the LINCS algorithm (*67*) to constrain all hydrogen-heavy atom bonds. Nonbonded interactions were calculated using the particle mesh Ewald (PME) method and a Verlet scheme, with a single cutoff of 1.4 nm for both the van der Waals and PME real-space sum.

Development of a Gram-positive model bilayer

To embed PsaBC in a near-native lipid environment, a Gram-positive bacterial membrane was constructed on the basis of the lipid composition of *S. pneumoniae*, composed primarily of anionic lipid species PG and CDL (*16*–*18*). The PG-to-CDL ratio was determined to be ~2:1, based on radiolabeling studies of P headgroups in PG and CDL (*18*). Saturated and monounsaturated acyl tail lengths of 18, 16, and 14 carbons are the most abundant in *S. pneumoniae* (*68*). To satisfy the PG:CDL ratio and most abundant tails, a five-component PG and CDL bilayer was used. The 1-palmitoyl-2-oleoyl-*sn*-glycero-3-phosphoglycerol (POPG) parameters defined by Kukol (*69*) were used to construct the following three PG species: PG1(18Δ7,16), PG2(18Δ7,18), and PG3(14,16). Torsionals defined by Bachar and co-workers (*70*) were incorporated at unsaturated positions. CDL species were obtained by joining two molecules of PG, and any missing parameters were obtained from the GROMOS 54A7 parameter set (*62*). The following CDL species were constructed for use in the model bilayer: CDL1(14,16,16Δ9,16) and CDL2(16,16Δ7,18Δ9,18). Final ratios for the lipid species were 2:1:1:1:1 for PG1, PG2, PG3, CL1, and CL2, respectively. Individual lipids were energy minimized in vacuo using the steepest descent minimization. A small system with inter-leaflet symmetry and a total of 108 lipids (54 per leaflet) were prepared for equilibration. The system was solvated with approximately 85 simple point charge (SPC) model waters per lipid to ensure equilibration of solvent dynamics at the lipid interface and neutralized with sodium ions. A 250-ns simulation was conducted to equilibrate the small bilayer. The equilibrated small bilayer was then tiled to form a larger bilayer system with 972 lipids in total and was resolvated in a larger cubic box of SPC water and reneutralized. The larger system was then simulated for 250 ns to allow for further equilibration using the same method described above.

Preparation of PsaBC simulation systems

MD simulations were performed on the biological assembly of $^{\mathrm{F100S}}$PsaBC, starting from $^{\mathrm{F100S}}$PsaBC crystallized in the absence of Fab. Unresolved residues in each of the two $^{\mathrm{F100S}}$PsaBC structures were repaired in SwissPDBview (*71*). The extended cytoplasmic loop of PsaC was symmetrized between chains E and H of the crystal structure by grafting the loop from chain E onto chain H and conducting loop minimization in SwissPDBview. Furthermore, in this symmetrized $^{\mathrm{F100S}}$PsaBC structure, the reverse S100F mutation was performed with SwissPDBview to give $^{\mathrm{WT}}$PsaBC. A separate simulation system was set up for $^{\mathrm{F100S}}$PsaBC and $^{\mathrm{WT}}$PsaBC using the same overall procedure. In each case, a copy of PsaBC was embedded in a 500-lipid patch of the Gram-positive bilayer model described above, using the program InflateGro2 (*72*). The system was solvated, and counterions were added to ensure charge neutrality and a 150 mM NaCl concentration before energy minimization. The system was then relaxed in the bilayer using a series of position-restrained simulations. Here, series of 4-ns simulations were performed where position restraints were placed on all protein heavy atoms using successively decreasing force constants of 500 kJ mol^{-1} nm^{-2}, 250 mol^{-1} nm^{-2}, 100 kJ mol^{-1} nm^{-2}, and 50 kJ mol^{-1} nm^{-2}. The relaxed structures were given new velocities and simulated for eight replicates of 500 ns.

MD analyses

Root mean squared deviation

The RMSD was calculated using the Kabsch algorithm (*73*), which calculates the optimal rotation matrix that minimizes the RMSD between two paired sets of points.

Cluster analysis

The unrestrained trajectories for all independent simulation repeats initiated from $^{\mathrm{F100S}}$PsaBC crystallized without Fab and the $^{\mathrm{WT}}$PsaBC model were concatenated into a single combined trajectory file. To determine the relative populations of specific conformations sampled, the trajectories were clustered using the method of Daura and co-workers (*74*). Two conformations were considered neighbors if the backbone RMSD between the two conformations was <0.30 nm.

Solvent number volume analysis

Volumetric analysis was conducted using an in-house Python script, using the MDTraj 1.9 library (*75*). Briefly, a vector between the center of mass of two groups of residues is defined, giving the vector over which the water density is evaluated. A set of grid points (N_{grid}) is chosen along the vector. At each point, a disc of a specified radial width R is computed and the solvent number density within this disc assigned to the corresponding grid interval. Over the total grid, this approach calculates the solvent number density in a cylinder of specified radius R, with resolution N_{grid} along the vector. This process is calculated for each frame of the simulation. To evaluate the solvent number density within the PsaBC coordination site, the two groups used were Asp^{135} from chain F/H and Ser^{92} from chain F/H with $N_{\mathrm{grid}} = 20$ and radial width of 7 Å.

SUPPLEMENTARY MATERIALS

Supplementary material for this article is available at http://advances.sciencemag.org/cgi/content/full/7/32/eabg3980/DC1

View/request a protocol for this paper from *Bio-protocol*.

REFERENCES AND NOTES

1. K. J. Waldron, J. C. Rutherford, D. Ford, N. J. Robinson, Metalloproteins and metal sensing. *Nature* **460**, 823–830 (2009).
2. C. Andreini, I. Bertini, G. Cavallaro, G. L. Holliday, J. M. Thornton, Metal ions in biological catalysis: From enzyme databases to general principles. *J. Biol. Inorg. Chem.* **13**, 1205–1218 (2008).
3. K. M. Papp-Wallace, M. E. Maguire, Manganese transport and the role of manganese in virulence. *Annu. Rev. Microbiol.* **60**, 187–209 (2006).
4. J. R. Morey, C. A. McDevitt, T. E. Kehl-Fie, Host-imposed manganese starvation of invading pathogens: Two routes to the same destination. *Biometals* **28**, 509–519 (2015).
5. R. P. Berntsson, S. H. Smits, L. Schmitt, D.-J. Slotboom, B. Poolman, A structural classification of substrate-binding proteins. *FEBS Lett.* **584**, 2606–2617 (2010).
6. D. C. Rees, E. Johnson, O. Lewinson, ABC transporters: The power to change. *Nat. Rev. Mol. Cell Biol.* **10**, 218–227 (2009).
7. R. A. Gladstone, S. W. Lo, J. A. Lees, N. J. Croucher, A. J. Van Tonder, J. Corander, A. J. Page, P. Marttinen, L. J. Bentley, T. J. Ochoa, P. L. Ho, M. du Plessis, J. E. Cornick, B. Kwambana-Adams, R. Benisty, S. A. Nzenze, S. A. Madhi, P. A. Hawkins, D. B. Everett, M. Antonio, R. Dagan, K. P. Klugman, A. von Gottberg, L. M. Gee, R. F. Breiman, S. D. Bentley; Global Pneumococcal Sequencing Consortium, International genomic definition of pneumococcal lineages, to contextualise disease, antibiotic resistance and vaccine impact. *EBioMedicine* **43**, 338–346 (2019).
8. R. M. Couñago, M. P. Ween, S. L. Begg, M. Bajaj, J. Zuegg, M. L. O'Mara, M. A. Cooper, A. G. McEwan, J. C. Paton, B. Kobe, C. A. McDevitt, Imperfect coordination chemistry facilitates metal ion release in the Psa permease. *Nat. Chem. Biol.* **10**, 35–41 (2014).
9. M. de Boer, G. Gouridis, R. Vietrov, S. L. Begg, G. K. Schuurman-Wolters, F. Husada, N. Eleftheriadis, B. Poolman, C. A. McDevitt, T. Cordes, Conformational and dynamic plasticity in substrate-binding proteins underlies selective transport in ABC importers. *eLife* **8**, e44652 (2019).
10. V. B. Chen, W. B. Arendall III, J. J. Headd, D. A. Keedy, R. M. Immormino, G. J. Kapral, L. W. Murray, J. S. Richardson, D. C. Richardson, MolProbity: All-atom structure validation for macromolecular crystallography. *Acta Crystallogr. D Biol. Crystallogr.* **66**, 12–21 (2010).
11. E. L. Borths, B. Poolman, R. N. Hvorup, K. P. Locher, D. C. Rees, In vitro functional characterization of BtuCD-F, the *Escherichia coli* ABC transporter for vitamin B12 uptake. *Biochemistry* **44**, 16301–16309 (2005).
12. J. S. Woo, A. Zeltina, B. A. Goetz, K. P. Locher, X-ray structure of the *Yersinia pestis* heme transporter HmuUV. *Nat. Struct. Mol. Biol.* **19**, 1310–1315 (2012).
13. E. Vigonsky, E. Ovcharenko, O. Lewinson, Two molybdate/tungstate ABC transporters that interact very differently with their substrate binding proteins. *Proc. Natl. Acad. Sci. U.S.A.* **110**, 5440–5445 (2013).
14. A. L. Davidson, H. A. Shuman, H. Nikaido, Mechanism of maltose transport in *Escherichia coli*: Transmembrane signaling by periplasmic binding proteins. *Proc. Natl. Acad. Sci. U.S.A.* **89**, 2360–2364 (1992).
15. H. MacDermott-Opeskin, C. A. McDevitt, M. L. O'Mara, Comparing nonbonded metal ion models in the divalent cation binding protein PsaA. *J. Chem. Theory Comput.* **16**, 1913–1923 (2020).
16. M. Meiers, C. Volz, J. Eisel, P. Maurer, B. Henrich, R. Hakenbeck, Altered lipid composition in *Streptococcus pneumoniae cpoA* mutants. *BMC Microbiol.* **14**, 12 (2014).
17. C. Sohlenkamp, O. Geiger, Bacterial membrane lipids: Diversity in structures and pathways. *FEMS Microbiol. Rev.* **40**, 133–159 (2016).
18. M. C. Trombe, M. A. Lanéelle, G. Lanéelle, Lipid composition of aminopterin-resistant and sensitive strains of *Streptococcus pneumoniae.* Effect of aminopterin inhibition. *Biochim. Biophys. Acta* **574**, 290–300 (1979).
19. Y. Naoe, N. Nakamura, A. Doi, M. Sawabe, H. Nakamura, Y. Shiro, H. Sugimoto, Crystal structure of bacterial haem importer complex in the inward-facing conformation. *Nat. Commun.* **7**, 13411 (2016).
20. H. W. Pinkett, A. T. Lee, P. Lum, K. P. Locher, D. C. Rees, An inward-facing conformation of a putative metal-chelate-type ABC transporter. *Science* **315**, 373–377 (2007).
21. V. M. Korkhov, S. A. Mireku, D. B. Veprintsev, K. P. Locher, Structure of AMP-PNP-bound BtuCD and mechanism of ATP-powered vitamin B12 transport by BtuCD-F. *Nat. Struct. Mol. Biol.* **21**, 1097–1099 (2014).
22. S. Udayalaxmi, M. R. Gangula, K. Ravikiran, P. Ettaiah, Investigation of manganese metal coordination in proteins: A comprehensive PDB analysis and quantum mechanical study. *Struct. Chem.* **31**, 1057–1064 (2020).
23. J. Wu, Z. Yan, Z. Li, C. Yan, S. Lu, M. Dong, N. Yan, Structure of the voltage-gated calcium channel Cav1.1 complex. *Science* **350**, aad2395 (2015).
24. A. Zhang, H. Yu, C. Liu, C. Song, The Ca^{2+} permeation mechanism of the ryanodine receptor revealed by a multi-site ion model. *Nat. Commun.* **11**, 922 (2020).
25. C. Toyoshima, M. Nakasako, H. Nomura, H. Ogawa, Crystal structure of the calcium pump of sarcoplasmic reticulum at 2.6 A resolution. *Nature* **405**, 647–655 (2000).
26. I. A. Ehrnstorfer, E. R. Geertsma, E. Pardon, J. Steyaert, R. Dutzler, Crystal structure of a SLC11 (NRAMP) transporter reveals the basis for transition-metal ion transport. *Nat. Struct. Mol. Biol.* **21**, 990–996 (2014).
27. C. Cubillas, P. Vinuesa, M. L. Tabche, A. García-de los Santos, Phylogenomic analysis of cation diffusion facilitator proteins uncovers $\mathrm{Ni}^{2+}/\mathrm{Co}^{2+}$ transporters. *Metallomics* **5**, 1634–1643 (2013).
28. J. E. Martin, D. P. Giedroc, Functional determinants of metal ion transport and selectivity in paralogous cation diffusion facilitator transporters CzcD and MntE in *Streptococcus pneumoniae*. *J. Bacteriol.* **198**, 1066–1076 (2016).
29. M. L. Oldham, D. Khare, F. A. Quiocho, A. L. Davidson, J. Chen, Crystal structure of a catalytic intermediate of the maltose transporter. *Nature* **450**, 515–521 (2007).
30. M. L. Oldham, J. Chen, Crystal structure of the maltose transporter in a pretranslocation intermediate state. *Science* **332**, 1202–1205 (2011).
31. K. P. Locher, Mechanistic diversity in ATP-binding cassette (ABC) transporters. *Nat. Struct. Mol. Biol.* **23**, 487–493 (2016).
32. K. P. Locher, A. T. Lee, D. C. Rees, The *E. coli* BtuCD structure: A framework for ABC transporter architecture and mechanism. *Science* **296**, 1091–1098 (2002).
33. A. J. Rice, A. Park, H. W. Pinkett, Diversity in ABC transporters: Type I, II and III importers. *Crit. Rev. Biochem. Mol. Biol.* **49**, 426–437 (2014).
34. S. El-Gebali, J. Mistry, A. Bateman, S. R. Eddy, A. Luciani, S. C. Potter, M. Qureshi, L. J. Richardson, G. A. Salazar, A. Smart, E. L. L. Sonnhammer, L. Hirsh, L. Paladin, D. Piovesan, S. C. E. Tosatto, R. D. Finn, The Pfam protein families database in 2019. *Nucleic Acids Res.* **47**, D427–D432 (2019).
35. A. L. Davidson, E. Dassa, C. Orelle, J. Chen, Structure, function, and evolution of bacterial ATP-binding cassette systems. *Microbiol. Mol. Biol. Rev.* **72**, 317–364 (2008).
36. M. Eisenhut, N. Hoecker, S. B. Schmidt, R. M. Basgaran, S. Flachbart, P. Jahns, T. Eser, S. Geimer, S. Husted, A. P. M. Weber, D. Leister, A. Schneider, The plastid envelope CHLOROPLAST MANGANESE TRANSPORTER1 is essential for manganese homeostasis in *Arabidopsis*. *Mol. Plant* **11**, 955–969 (2018).
37. Z. Bao, X. Qi, S. Hong, K. Xu, F. He, M. Zhang, J. Chen, D. Chao, W. Zhao, D. Li, J. Wang, P. Zhang, Structure and mechanism of a group-I cobalt energy coupling factor transporter. *Cell Res.* **27**, 675–687 (2017).
38. D. J. Sherman, M. B. Lazarus, L. Murphy, C. Liu, S. Walker, N. Ruiz, D. Kahne, Decoupling catalytic activity from biological function of the ATPase that powers lipopolysaccharide transport. *Proc. Natl. Acad. Sci. U.S.A.* **111**, 4982–4987 (2014).
39. C. Thomas, S. G. Aller, K. Beis, E. P. Carpenter, G. Chang, L. Chen, E. Dassa, M. Dean, F. D. Van Hoa, D. Ekiert, R. Ford, R. Gaudet, X. Gong, I. B. Holland, Y. Huang, D. K. Kahne, H. Kato, V. Koronakis, C. M. Koth, Y. Lee, O. Lewinson, R. Lill, E. Martinoia, S. Murakami, H. W. Pinkett, B. Poolman, D. Rosenbaum, B. Sarkadi, L. Schmitt, E. Schneider, Y. Shi, S. L. Shyng, D. J. Slotboom, E. Tajkhorshid, D. P. Tieleman, K. Ueda, A. Váradi, P. C. Wen, N. Yan, P. Zhang, H. Zheng, J. Zimmer, R. Tampé, Structural and functional diversity calls for a new classification of ABC transporters. *FEBS Lett.* **594**, 3767–3775 (2020).
40. C. K. Sung, H. Li, J. P. Claverys, D. A. Morrison, An *rpsL* cassette, janus, for gene replacement through negative selection in *Streptococcus pneumoniae*. *Appl. Environ. Microbiol.* **67**, 5190–5196 (2001).
41. C. D. Plumptre, B. A. Eijkelkamp, J. R. Morey, F. Behr, R. M. Couñago, A. D. Ogunniyi, B. Kobe, M. L. O'Mara, J. C. Paton, C. A. McDevitt, AdcA and AdcAII employ distinct zinc acquisition mechanisms and contribute additively to zinc homeostasis in *Streptococcus pneumoniae*. *Mol. Microbiol.* **91**, 834–851 (2014).
42. C. A. McDevitt, A. D. Ogunniyi, E. Valkov, M. C. Lawrence, B. Kobe, A. G. McEwan, J. C. Paton, A molecular mechanism for bacterial susceptibility to zinc. *PLOS Pathog.* **7**, e1002357 (2011).
43. G. S. Waldo, B. M. Standish, J. Berendzen, T. C. Terwilliger, Rapid protein-folding assay using green fluorescent protein. *Nat. Biotechnol.* **17**, 691–695 (1999).
44. S. L. Begg, B. A. Eijkelkamp, Z. Luo, R. M. Counago, J. R. Morey, M. J. Maher, C. L. Ong, A. G. McEwan, B. Kobe, M. L. O'Mara, J. C. Paton, C. A. McDevitt, Dysregulation

of transition metal ion homeostasis is the molecular basis for cadmium toxicity in *Streptococcus pneumoniae*. *Nat. Commun.* **6**, 6418 (2015).
45. F. Jaenecke, Y. Nakada-Nakura, K. Nagarathinam, S. Ogasawara, K. Liu, Y. Hotta, S. Iwata, N. Nomura, M. Tanabe, Generation of conformation-specific antibody fragments for crystallization of the multidrug resistance transporter MdfA. *Methods Mol. Biol.* **1700**, 97–109 (2018).
46. S. Newstead, S. Ferrandon, S. Iwata, Rationalizing alpha-helical membrane protein crystallization. *Protein Sci.* **17**, 466–472 (2008).
47. J. L. Parker, S. Newstead, Current trends in α-helical membrane protein crystallization: An update. *Protein Sci.* **21**, 1358–1365 (2012).
48. Z. Otwinowski, W. Minor, [20] Processing of x-ray diffraction data collected in oscillation mode. *Methods Enzymol.* **276**, 307–326 (1997).
49. J. D. Ye, V. Tereshko, J. K. Frederiksen, A. Koide, F. A. Fellouse, S. S. Sidhu, S. Koide, A. A. Kossiakoff, J. A. Piccirilli, Synthetic antibodies for specific recognition and crystallization of structured RNA. *Proc. Natl. Acad. Sci. U.S.A.* **105**, 82–87 (2008).
50. P. Emsley, K. Cowtan, *Coot*: Model-building tools for molecular graphics. *Acta Crystallogr. D* **60**, 2126–2132 (2004).
51. E. R. Geertsma, N. A. Nik Mahmood, G. K. Schuurman-Wolters, B. Poolman, Membrane reconstitution of ABC transporters and assays of translocator function. *Nat. Protoc.* **3**, 256–266 (2008).
52. A. J. Page, N. De Silva, M. Hunt, M. A. Quail, J. Parkhill, S. R. Harris, T. D. Otto, J. A. Keane, Robust high-throughput prokaryote de novo assembly and improvement pipeline for Illumina data. *Microb. Genom.* **2**, e000083 (2016).
53. M. R. Davies, L. McIntyre, A. Mutreja, J. A. Lacey, J. A. Lees, R. J. Towers, S. Duchêne, P. R. Smeesters, H. R. Frost, D. J. Price, M. T. G. Holden, S. David, P. M. Giffard, K. A. Worthing, A. C. Seale, J. A. Berkley, S. R. Harris, T. Rivera-Hernandez, O. Berking, A. J. Cork, R. S. L. A. Torres, T. Lithgow, R. A. Strugnell, R. Bergmann, P. Nitsche-Schmitz, G. S. Chhatwal, S. D. Bentley, J. D. Fraser, N. J. Moreland, J. R. Carapetis, A. C. Steer, J. Parkhill, A. Saul, D. A. Williamson, B. J. Currie, S. Y. C. Tong, G. Dougan, M. J. Walker, Atlas of group A streptococcal vaccine candidates compiled using large-scale comparative genomics. *Nat. Genet.* **51**, 1035–1043 (2019).
54. M. Kearse, R. Moir, A. Wilson, S. Stones-Havas, M. Cheung, S. Sturrock, S. Buxton, A. Cooper, S. Markowitz, C. Duran, T. Thierer, B. Ashton, P. Meintjes, A. Drummond, Geneious Basic: An integrated and extendable desktop software platform for the organization and analysis of sequence data. *Bioinformatics* **28**, 1647–1649 (2012).
55. R. C. Edgar, MUSCLE: Multiple sequence alignment with high accuracy and high throughput. *Nucleic Acids Res.* **32**, 1792–1797 (2004).
56. E. F. Pettersen, T. D. Goddard, C. C. Huang, G. S. Couch, D. M. Greenblatt, E. C. Meng, T. E. Ferrin, UCSF Chimera—A visualization system for exploratory research and analysis. *J. Comput. Chem.* **25**, 1605–1612 (2004).
57. T. J. Wheeler, J. Clements, R. D. Finn, Skylign: A tool for creating informative, interactive logos representing sequence alignments and profile hidden Markov models. *BMC Bioinformatics* **15**, 7 (2014).
58. A. M. Waterhouse, J. B. Procter, D. M. Martin, M. Clamp, G. J. Barton, Jalview Version 2—A multiple sequence alignment editor and analysis workbench. *Bioinformatics* **25**, 1189–1191 (2009).
59. H. J. C. Berendsen, D. van der Spoel, R. van Drunen, GROMACS: A message-passing parallel molecular dynamics implementation. *Comput. Phys. Commun.* **91**, 43–56 (1995).
60. M. J. Abraham, T. Murtola, R. Schulz, S. Páll, J. C. Smith, B. Hess, E. Lindah, Gromacs: High performance molecular simulations through multi-level parallelism from laptops to supercomputers. *SoftwareX* **1-2**, 19–25 (2015).
61. D. Van Der Spoel, E. Lindahl, B. Hess, G. Groenhof, A. E. Mark, H. J. C. Berendsen, GROMACS: Fast, flexible, and free. *J. Comput. Chem.* **26**, 1701–1718 (2005).
62. N. Schmid, A. P. Eichenberger, A. Choutko, S. Riniker, M. Winger, A. E. Mark, W. F. van Gunsteren, Definition and testing of the GROMOS force-field versions 54A7 and 54B7. *Eur. Biophys. J.* **40**, 843–856 (2011).
63. G. Bussi, D. Donadio, M. Parrinello, Canonical sampling through velocity rescaling. *J. Chem. Phys.* **126**, 014101 (2007).
64. H. J. C. Berendsen, J. P. M. Postma, W. F. Van Gunsteren, A. Dinola, J. R. Haak, Molecular dynamics with coupling to an external bath. *J. Chem. Phys.* **81**, 3684–3690 (1984).
65. M. Parrinello, A. Rahman, Polymorphic transitions in single crystals: A new molecular dynamics method. *J. App. Phys.* **52**, 7182–7190 (1981).
66. M. Parrinello, A. Rahman, Crystal structure and pair potentials: A molecular-dynamics study. *Phys. Rev. Lett.* **45**, 1196–1199 (1980).
67. B. Hess, H. Bekker, H. J. C. Berendsen, J. G. E. M. Fraaije, LINCS: A Linear Constraint Solver for molecular simulations. *J. Comput. Chem.* **18**, 1463–1472 (1997).
68. T. Gutberlet, U. Dietrich, H. Bradaczek, G. Pohlentz, K. Leopold, W. Fischer, Cardiolipin, α-D-glucopyranosyl, and L-lysylcardiolipin from Gram-positive bacteria: FAB MS, monofilm and x-ray powder diffraction studies. *Biochim. Biophys. Acta* **1463**, 307–322 (2000).
69. A. Kukol, Lipid models for united-atom molecular dynamics simulations of proteins. *J. Chem. Theory Comput.* **5**, 615–626 (2009).
70. M. Bachar, P. Brunelle, D. P. Tieleman, A. Rauk, Molecular dynamics simulation of a polyunsaturated lipid bilayer susceptible to lipid peroxidation. *J. Phys. Chem. B* **108**, 7170–7179 (2004).
71. N. Guex, M. C. Peitsch, SWISS-MODEL and the Swiss-PdbViewer: An environment for comparative protein modeling. *Electrophoresis* **18**, 2714–2723 (1997).
72. T. H. Schmidt, C. Kandt, LAMBADA and InflateGRO2: Efficient membrane alignment and insertion of membrane proteins for molecular dynamics simulations. *J. Chem. Inf. Model.* **52**, 2657–2669 (2012).
73. W. Kabsch, A discussion of the solution for the best rotation to relate two sets of vectors. *Acta Crystallogr. A* **34**, 827–828 (1978).
74. X. Daura, K. Gademann, B. Jaun, D. Seebach, W. F. van Gunsteren, A. E. Mark, Peptide folding: When simulation meets experiment. *Angew Chem.* **38**, 236–240 (1999).
75. R. T. McGibbon, K. A. Beauchamp, M. P. Harrigan, C. Klein, J. M. Swails, C. X. Hernández, C. R. Schwantes, L. P. Wang, T. J. Lane, V. S. Pande, MDTraj: A modern open library for the analysis of molecular dynamics trajectories. *Biophys. J.* **109**, 1528–1532 (2015).

Acknowledgments: We thank the SSRL beamline staff for the enthusiastic and professional support. In particular, we express our thanks to T. Doukov, who went to extraordinary lengths to ensure that our samples arrived at the SSRL safely. We also thank Y. Nakada-Nakura, K. Liu, and T. Uemura for technical assistance in the generation of antibodies and P. Shilling for assistance in PsaBC protein expression and purification. **Funding:** This work was supported by the National Health and Medical Research Council (NHMRC) Project grants 1080784 to C.A.M. and M.J.M.; 1140554 to C.A.M., M.J.M., and M.L.O.; and 1122582 to C.A.M.; an Australian Research Council (ARC) Discovery Project grant DP170102102 to C.A.M.; and funding from the Platform Project for Supporting Drug Discovery and Life Science Research [Basis for Supporting Innovative Drug Discovery and Life Science Research (BINDS)] from AMED under grant number JP20am0101079 to S.I. (support number 0752). S.L.N. is an NHMRC Early Career Research Fellow (1142695), M.R.D. is a University of Melbourne C. R. Roper Fellow, and C.A.M. and M.J.M. are ARC Future Fellows (FT170100006 and FT180100397, respectively). Part of this study was carried out using the 12-2 beamline at the Stanford Synchrotron Radiation Laboratory (SSRL). We acknowledge travel funding provided by the International Synchrotron Access Program (ISAP) managed by the Australian Synchrotron, part of ANSTO, and funded by the Australian Government. Use of the Stanford Synchrotron Radiation Lightsource, SLAC National Accelerator Laboratory, is supported by the U.S. Department of Energy, Office of Sciences, under contract no. DE-AC02-76SF00515. The SSRL Structural Molecular Biology Program is supported by the DOE Office of Biological and Environmental Research and by the NIH, National Institute of General Medical Sciences (PG0GM133894). The research was undertaken with the assistance of resources and services from the National Computational Infrastructure (NCI), which is supported by the Australian Government, and using the LIEF HPC-GPGPU Facility hosted at the University of Melbourne, established with the assistance of LIEF grant LE170100200. Molecular graphics and analyses were performed with UCSF Chimera, developed by the Resource for Biocomputing, Visualization, and Informatics at the University of California, San Francisco, with support from NIH P41-GM103311. The contents of this publication are solely the responsibility of the authors and do not necessarily represent the official views of NIGMS or NIH. **Author contributions:** S.L.N., J.S., J.A.W., H.M.-O., S.J.F., K.G., A.C.H., A.P.M., A.J.H., T.R.M., M.R.D., N.N., S.I., M.L.O., M.J.M., and C.A.M. designed experiments. S.L.N. and J.A.W. conducted the microbiological and biochemical assays. J.S., T.R.M., and M.J.M. performed the structural studies. H.M.-O., S.J.F., and M.L.O. performed the MD simulations and analyses. K.G. performed the ICP-MS analyses. A.C.H. developed the reconstitution procedure. S.L.N. and A.C.H. generated *S. pneumoniae* mutant variant strains. A.P.M., A.C.H., and J.A.W. generated expression constructs. S.L.N., A.J.H., and M.R.D. performed bioinformatic analyses. N.N. and S.I. generated the Fabs. M.J.M. and C.A.M. conceived and designed the study and wrote the manuscript. All authors reviewed the manuscript. **Competing interests:** The authors declare that they have no competing interests. **Data and materials availability:** All data needed to evaluate the conclusions in the paper are present in the paper and/or the Supplementary Materials. The ^{F100S}PsaBC-Fab and ^{F100S}PsaBC coordinates have been deposited with the Protein Data Bank with the accession codes 7KYO and 7KYP, respectively. Additional data related to this paper may be requested from the authors.

Submitted 4 January 2021
Accepted 10 June 2021
Published 6 August 2021
10.1126/sciadv.abg3980

Citation: S. L. Neville, J. Sjöhamn, J. A. Watts, H. MacDermott-Opeskin, S. J. Fairweather, K. Ganio, A. Carey Hulyer, A. P. McGrath, A. J. Hayes, T. R. Malcolm, M. R. Davies, N. Nomura, S. Iwata, M. L. O'Mara, M. J. Maher, C. A. McDevitt, The structural basis of bacterial manganese import. *Sci. Adv.* **7**, eabg3980 (2021).